Detection of Strong Light−Matter Interaction in a Single Nanocavity with a Thermal Transducer

Mario Malerba,*,[¶] Simone Sotgiu,[¶] Andrea Schirato, Leonetta Baldassarre, Raymond Gillibert, Valeria Giliberti, Mathieu Jeannin, Jean-Michel Manceau, Lianhe Li, Alexander Giles Davies, Edmund H. Linfield, Alessandro Alabastri, Michele Ortolani,* and Raffaele Colombelli*

ACCESS | 📊 Metrics & More | 📑 Article Recommendations | 🆂🅸 Supporting Information

ABSTRACT: The concept of strong light−matter coupling has been demonstrated in semiconductor structures, and it is poised to revolutionize the design and implementation of components, including solid state lasers and detectors. We demonstrate an original nanospectroscopy technique that permits the study of the light−matter interaction in single subwavelength-sized nanocavities where far-field spectroscopy is not possible using conventional techniques. We inserted a thin (~150 nm) polymer layer with negligible absorption in the mid-infrared range (5 μm < λ < 12 μm) inside a metal−insulator−metal resonant cavity, where a photonic mode and the intersubband transition of a semiconductor quantum well are strongly coupled. The intersubband

transition peaks at λ = 8.3 μm, and the nanocavity is overall 270 nm thick. Acting as a nonperturbative transducer, the polymer layer introduces only a limited alteration of the optical response while allowing to reveal the optical power absorbed inside the concealed cavity. Spectroscopy of the cavity losses is enabled by the polymer thermal expansion due to heat dissipation in the active part of the cavity, and performed using atomic force microscopy (AFM). This innovative approach allows the typical anticrossing characteristic of the polaritonic dispersion to be identified in the cavity loss spectra at the single nanoresonator level. Results also suggest that near-field coupling of the external drive field to the top metal patch mediated by a metal-coated AFM probe tip is possible, and it enables the near-field mapping of the cavity mode symmetry including in the presence of a strong light−matter interaction.

KEYWORDS: *intersubband transition, strong coupling, patch nanoantenna, optical nanocavity, IR nanospectroscopy, mid-IR*
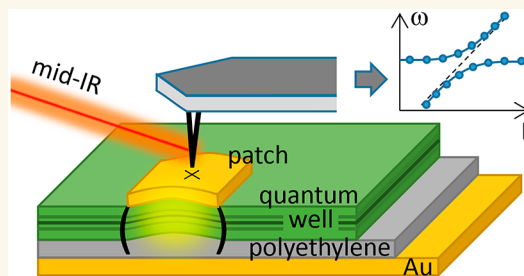
P hotonic devices are increasingly developed based on a meta-material approach, where the device functionality stems from the properties of subwavelength units/resonators (meta-atoms) that make up the whole optical nanostructured material. The optical response is defined by design obtaining meta-materials,[1] meta-surfaces[2,3] or nonlinear surfaces.[4−7] The unit elements of meta-materials have subwavelength dimensions, and they usually operate independently from neighboring units. For this reason, the spectroscopic study of single subwavelength units represents an important tool for the development and understanding of such systems: single-object spectroscopy, as opposed to the far-field spectroscopy study of the collective response of large resonator arrays, is enabled by fiber-based or aperture-less scanning near-field optical microscopy (SNOM).[8,9] The electromagnetic (EM) near field plays a crucial role in the

operation of meta-materials, and SNOM also permits one to image near fields.

In the mid-infrared (IR) and THz spectral ranges, meta-material approaches have recently attracted interest too. On the one hand, the reasonably low ohmic losses at long infrared wavelengths allow the use of metallic meta-structures without introducing excessive damping. This explains why meta-surfaces embedding active materials (detectors,[10,11] lasers/emitters,[12] modulators[13]) have been employed successfully. On the other hand, the extreme confinement enabled by
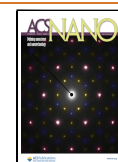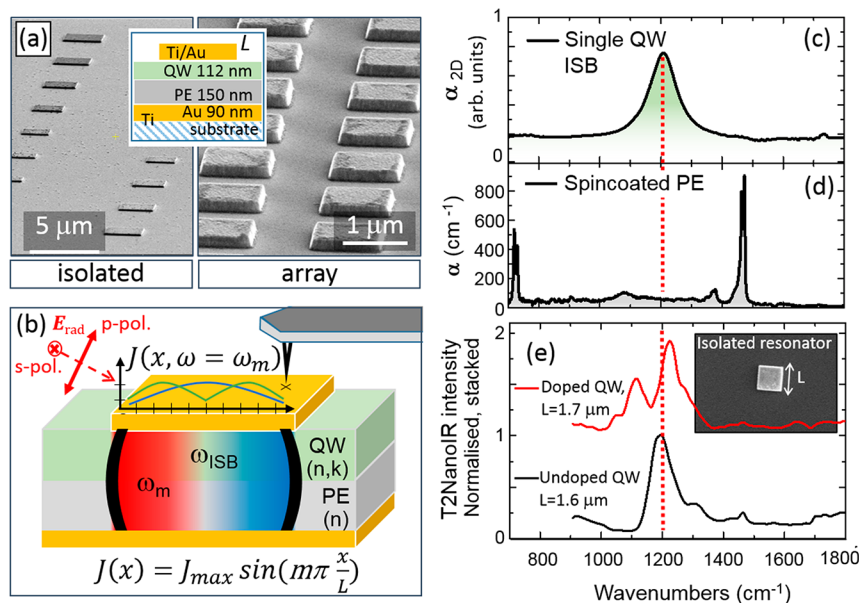
Figure 1. (a) SEM images taken on different areas of the same chip after device nanofabrication. Left panel: a set of isolated square-patch nanocavities with different values of lateral side L (the distance between neighboring cavities is $>20L$). Right panel: an array of quasi-independent cavities with period $P = 2L$ to be used for far-field spectroscopy. Inset: layer structure of the chip, QW: quantum well; PE: polyethylene; Au: evaporated gold patches and ground plane. The thickness values have been measured from cross sections obtained by focused ion beam milling. (b) Sketch of the T2NanoIR illumination scheme on a single nanocavity and definition of the main physical quantities involved: ω_m is the photonic cavity mode resonance frequency; ω_{ISB} is the intersubband transition frequency in the semiconductor QW; $J_x(\omega_m)$ is the x-component of the electric-current standing-wave pattern on the square patch at the mth mode. (c) Absorption spectrum of the doped QW measured by FTIR multipass transmission spectroscopy. The red dotted vertical line highlights the frequency of the ISB transition. (d) Absorption coefficient of a PE film spin-coated on gold inferred from its FTIR reflectivity. (e) T2Nano-IR spectra of single nanocavities, in the case of an undoped (black curve) and doped (red curve) active region. The former reveals the bare cavity resonance, the latter reveals the two polariton branches.

metal−insulator−metal (MIM) structures permits the study of cavity electrodynamics phenomena, particularly to achieve the regime known as the strong light−matter interaction. This is a peculiar condition of interaction between photonic and matter states, of interest not only for fundamental physics[14,15] but also because of its potential for improving optoelectronic devices in the mid-IR and THz spectral regions.[13,16−18]

If we consider square patch nanoantennas (a textbook example of an MIM resonant cavity[19]), optical measurements in the far-field require arrays of tens to hundreds of nanocavities to obtain a good signal-to-noise ratio. There are very few reports of single nanocavity studies at long infrared wavelengths,[20,21] mostly due to the rather large diffraction limit, and to the inefficiency of mid-IR and especially THz detectors. Furthermore, in patch antennas the core of the architecture—the active region within the optical cavity, where the light−matter interaction takes place—is concealed by the top metal patch and therefore is inaccessible to direct near-field investigation. Optically targeting one single resonator, and simultaneously accessing the concealed active cavity core, thus remains far from straightforward in these conditions.

RESULTS AND DISCUSSION

In this work, we present an alternative approach to scattering SNOM,[22,23] based on photothermal expansion detection with an atomic force microscopy (AFM) probe.[24−27] Our approach is capable of detecting the spectral response of a single MIM cavity in the mid-IR range, both in the weak- and strong-coupling regimes. In contrast to SNOM techniques that probe fringing fields leaking outside the cavity and scattered/

collected by the probe, our technique is only sensitive to the losses produced by the oscillation of the intracavity field, via the generated heating, and can therefore operate even in the ideal case when the electromagnetic field is fully localized inside the cavity, as in MIM resonant cavities. Photothermal simulations reproduce the experimental loss spectra and enable the observed photothermal expansion to be linked to the different heat sources in the system. Our technique is also capable of imaging different nanoscale patterns of electric current at the optical frequencies connected to the different resonant modes of the cavities.

The core idea of our approach is summarized in Figure 1: we have fabricated different isolated nanocavities and large arrays of identical nanocavities on the same chips (Figure 1a) to compare the spectroscopy results of our single nanocavity technique to those of conventional far-field reflection spectroscopy performed on large arrays. In the inset of Figure 1a, a cross section of the surface layers shows the MIM cavity embedding an active region which, as in traditional studies of strong light−matter coupling regime in the mid-IR, is made of a doped semiconductor quantum well (QW) featuring mid-IR intersubband (ISB) transitions.[28] The ISB transitions provide high oscillator strengths in the mid-IR and THz spectral ranges, and are the backbone principle behind the quantum cascade laser[29] and the quantum well infrared photodetector.[30] ISB transitions are also relevant for studies of fundamental physical phenomena at very long wavelengths. If the light−matter interaction is stronger than the dephasing mechanisms in the system, new quasi-particles, called ISB polaritons, emerge.[31,16] ISB polaritons have been studied theoretically and experimentally recently, with developments including ISB

polariton LEDs,[32,33] ultrafast switching,[34] ultrastrongly coupled systems,[35,36] and polariton-based detectors.[17,37] All these results have been obtained with highly confining MIM cavities embedding the active region with an EM overlap approaching unity. The technical innovation introduced here consists of an intracavity thin layer of polyethylene (PE) that serves as a thermal insulation layer of the active part of the cavity from the heat sink constituted by the substrate, and simultaneously serves as the main thermal expansion layer, thereby amplifying the photoexpansion signal of semiconductor and metal layers above it, which would be too small to be detected by AFM. This large amplification widely compensates the partial loss of EM overlap by a factor of 2 or less between the cavity field and the QW active region. The PE layer acts as a transducer: it receives heat and expands, and such expansion is detected by AFM. Hereafter, we will refer to our technique as thermal transducer NanoIR (T2NanoIR). A similar technique has been previously employed for much simpler planar circuits in refs 8 and 26, but in our work the expansion layer is positioned inside a cavity to detect the heat generated therein. The lateral resolution of heat detection is obviously not limited by diffraction but rather by heat diffusion, which is here carefully engineered to enable spectroscopy of a single nanocavity (see the Supporting Information).

In this respect, our technique belongs to the family of techniques that image optical near-fields by detecting non-optical imprints in the material.[38−40] If inserting a polymer layer in the device structure may appear like a complicated and unnecessary process step, the T2NanoIR technique may be of interest in the context of device physics and technology. In fact, it is not uncommon in the microelectronic industry to plan and implement "dummy wafer" microfabrication runs, in which transistor and diode structures are produced for the sole purpose of studying the thermal dissipation. Besides, the insensitivity of T2NanoIR, if compared to SNOM, to the scattering of the driving laser radiation by nearby photonic integrated circuit elements, including parts and edges of the cavity under study,[41] may become a key advantage of T2NanoIR in the field of nanophotonic device characterization (see the Supporting Information).

Figure 1b introduces the different quantities involved in the strong light−matter interaction in a single nanocavity. Metal (Ti/Au) layers are employed for optical confinement. The active region embedded in the MIM resonator is a single InGaAs/AlInAs QW, whose ISB absorption outside the cavity peaks at $\omega_{ISB} \sim 1180$ cm^{-1} (Figure 1c). The square patch nanocavity of side L, in the absence of a material with a dipole resonance in its internal volume, resonates at $\omega_m = 4\pi c/nmL$, where n is the effective refractive index of the dielectric material filling the cavity volume, c is the speed of light, and m = 1, 2, ... is an integer mode index. Assuming that the radiation electric field E_{rad} has a nonzero component along x, it is possible to infer the electric-current standing-wave pattern that forms on the square patch using the well-known two-curl combination of the third and fourth Maxwell's equations. The electric-current standing-wave patterns J_x ($\omega = \omega_m$) forming on the resonator for the first two modes m = 1 and m = 2 are sketched in Figure 1b (for completeness, we mention that 2D modes with simultaneous excitation along x and y are also possible in a two-dimensional square patch cavity, but we do not discuss them in this work). The ∼150 nm-thick PE layer is introduced in the cavity using an original nanofabrication technique, which separates the patterning of the active region

under study from the realization of the host transducer layer (see the Supporting Information). The measured PE absorption coefficient α_{PE} (Figure 1d) does not show any vibrational mode in the frequency range of interest, ideally avoiding the phenomenon of surface-enhanced infrared absorption (SEIRA) that has been exploited, e.g., in ref 26, for nanoscale imaging. In this sense the polymer purely acts as a transducer, and not as an active absorber.

When light from a tunable laser source (wavenumber ω) is focused on the sample, it is absorbed at the system resonance and dissipated via the different damping channels of the system (ISB absorption and metal ohmic losses). This heats up the material inside the cavity including the PE layer, which features a relatively high linear thermal expansion coefficient and a low thermal conductance that promotes the temperature increase inside the cavity volume ΔT. Scanning ω while simultaneously measuring the corresponding photothermal expansion with the AFM probe positioned on top of the patch antenna, the cavity loss spectrum can be recorded: it carries information on the single-cavity behavior. For example, in Figure 1e the T2NanoIR spectrum of a cavity loaded with an undoped QW not displaying any ISB transition (black curve) only shows the ohmic losses in the metal patch, which increase when the cavity is at the m = 1 resonant mode.

To demonstrate spectroscopy with the T2NanoIR technique on a single nanocavity, we chose a particularly challenging light−matter interaction condition: the strong coupling regime, where the electromagnetic environment plays a fundamental role in allowing (or preventing) the optical mode to interact strongly with the ISB transition. For the typical polaritonic anticrossing signature to be detected, the inserted polymer must not induce any important dephasing mechanism or negatively impact the EM overlap in the active region, hampering the coupling strength. Any non-negligible inter-action with the polymer would transition the system toward weak coupling. Therefore, a nonabsorbing transducer material must be used. The spectrum in Figure 1e obtained with the T2nanoIR technique on an isolated nanocavity loaded with an active doped QW (red curve) exemplifies the typical polariton splitting (or anticrossing behavior) observed in the far-field in nanocavity arrays when the cavity resonance matches the absorption resonance of the QW active region.

The signal-to-noise ratio of the T2NanoIR technique can be optimized by employing a gold-coated AFM probe tip in p-polarization at strongly oblique incidence (here 70°, see Figure 1b), a configuration that enhances the radiation field around the tip apex, and by pulsing the laser beam at a repetition rate around f = 150−250 kHz, matching one of the mechanical resonances of the AFM cantilever as discussed in ref 25. Quantum cascade lasers (QCLs) are currently the only mid-IR laser source that can provide single-mode pulsed excitation at any wavenumber and at any pulse repetition rate in the range of cantilever mechanical resonances. In this case, the T2NanoIR signal is the spectral component at f of the position-sensitive photodiode signal of the AFM optical lever, detected by lock-in amplification, and it is proportional, also via the quality factor of the mechanical resonance (usually around 100), to the actual photoexpansion of the sample under the AFM tip apex $\delta z(\omega)$. In turn, the latter is proportional to the total absorbed radiation power that is the sum of two terms: a direct far-field absorption of E_{rad} by the illuminated patch and a near-field absorption mediated by the enhanced fields around the gold-coated AFM tip. The dependences of

$\delta z(\omega)$ on the exact position (x,y) of the tip above the patch, on the laser polarization (p or s), and on the AFM tip-coating material (gold or dielectric) is found to be rather weak in the present case, indicating that near-field coupling through the tip is not the dominant energy transfer mechanism from the laser beam to the cavity. Therefore, the T2NanoIR spectra have been acquired by keeping the AFM tip at a fixed position at the center of the square patch, while scanning the wavenumber ω of the QCL beam. In our experiment, near-field coupling is unessential for single nanocavity spectroscopy, but nevertheless it is present and we will come back to this point at the end of the paper.

Having demonstrated in Figure 1e that high-quality cavity-loss spectra can be recorded on isolated nanocavities even in the strong light−matter interaction regime, we now turn to the comparison of the T2NanoIR spectra with more conventional far-field absorption spectra $A(\omega) = 1 - R(\omega)$ where the reflectivity $R(\omega)$ is measured with Fourier Transform IR (FTIR) microspectroscopy techniques. Signal-to-noise and diffraction limitations require that arrays of at least a hundred of uncoupled identical nanocavities be fabricated for FTIR analysis.

Figure 2 reports the spectral comparison between absorption spectra in the far-field on an ensemble of nominally identical patch resonators, and T2Nano-IR spectra on a single nanocavity belonging to the ensemble. The samples comprise arrays of square patch nanoantennas, with side dimensions L in the range 1.0−2.0 μm, fabricated according to the scheme in Figure 1b. For control, the T2NanoIR spectra have been acquired on several nanocavities for each array labeled with L and the difference in spectra have been found to be not significant (see the Supporting Information).

Figure 2a shows the measurements on an undoped sample (same active region, but no QW doping). The gray lines are the normalized $A(\omega)$ measured in the far-field. The T2NanoIR cavity loss spectra (orange curves) reasonably overlap with the corresponding $A(\omega)$. In panel a, the fundamental $m = 1$ cavity mode is visible for all values of L, and it correctly blue-shifts with decreasing L.[42] In the samples with longer L, the second order one-dimensional mode with $m = 2$ appears at higher wavenumbers, as expected. The minor differences between T2NanoIR cavity loss spectra and the far-field absorption spectra are not systematic and can be attributed to deviation from the perfect square shape of some of the patches and/or unwanted SEIRA effect due to vibrational absorption by chemical impurities in the PE layer or by lithography process residues. As shown in Figure 2c, the thermal transducer enables the same loss spectrum to be captured on a single cavity, and we can confirm that, in the undoped QW samples of Figures 2a,c, $\delta z(\omega)$ is proportional to the ohmic metal losses only.

Figure 2b,d reports the measurements on the doped QW sample (the InGaAs layer is doped with Si to 10^{19} cm^{-3}): the ISB transition, clearly resolved in the two extremal samples $L =$ 1.0 μm and $L =$ 2.0 μm, interacts with the fundamental cavity mode producing, at all other L's, variations of the cavity loss spectrum from the simple sum of noninteracting ohmic and ISB losses. The vertical dotted line at 1180 cm^{-1} corresponds to the position of the ISB absorption peak of Figure 1c. A clear anticrossing behavior, with a minimum polariton splitting obtained for $L =$ 1.6 μm, is observed with both techniques and this is clear proof of the strong light−matter interaction regime, even on single isolated nanocavities (Figure 2d). A
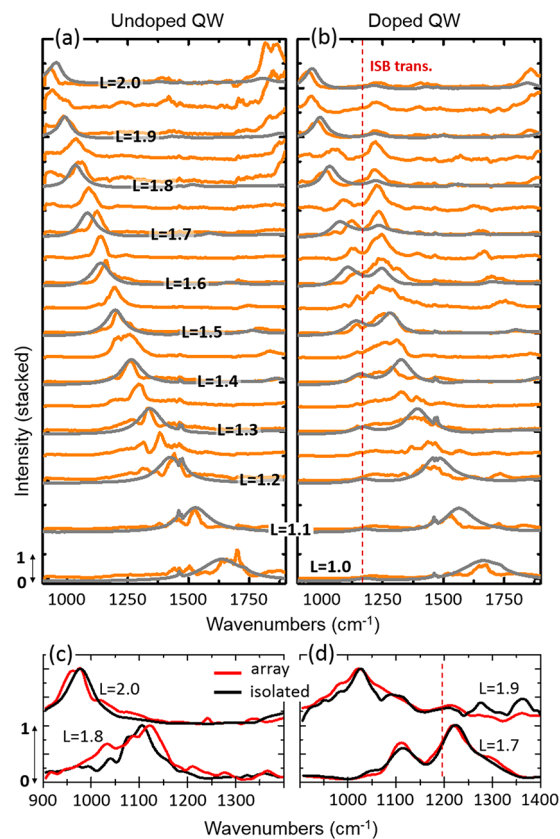

Figure 2. T2Nano-IR photoexpansion spectra (orange lines) of individual patch cavities compared to FTIR absorption spectra obtained from reflectivity measurements on the entire arrays (gray lines) for different patch side L. (a) Spectra obtained on cavities loaded with an undoped QW, thus exhibiting purely photonic cavity modes. (b) Spectra measured on cavities loaded with a doped ($n = 10^{19}$ cm^{-3}) QW, exhibiting a polaritonic behavior and an anticrossing at the ISB transition frequency. (c,d) Comparison of T2Nano-IR aborption spectra taken on isolated patch cavities compared to that taken on cavities belonging to large arrays: (c) undoped and (d) doped QWs. The minor spectral differences that can be found, like the one for the undoped $L = 1.8$ μm cavities around 1040 cm^{-1}, can be ascribed to unwanted SEIRA effect from vibrational absorption by chemical impurities in the PE layer or by nanofabrication process residues.

summary of the spectral peak positions is reported in Figure 3: it confirms the overall agreement between far-field (FTIR) and near-field (T2Nano-IR) data for both the undoped QW (Figure 3a) and the doped QW operating in the strong light−matter interaction regime (Figure 3b). In the background the coupled-mode theory calculation of the cavity loss spectrum is plotted in the form of underlaying grayscale image. From Figure 3b we can obtain the vacuum Rabi splitting $2\Omega_{\text{Rabi}}$, which is defined as twice the Rabi frequency: $2\Omega_{\text{Rabi}} = 125$ cm^{-1} (3.8 THz or 15 meV). It is exactly the same when calculated from T2NanoIR or from FTIR data.

Once we have demonstrated that cavity loss spectra can be equally obtained from far-field reflection spectroscopy in large arrays and from T2NanoIR spectroscopy on isolated (or single) cavities, we can proceed to determine the origin of the temperature increase ΔT that produces the T2NanoIR signal in both the undoped and doped QW samples. Indeed, the quantity $\delta z(\omega)$ peaks approximately at the same ω as the cavity losses (Figure 3) but its spectral intensity will depend on the
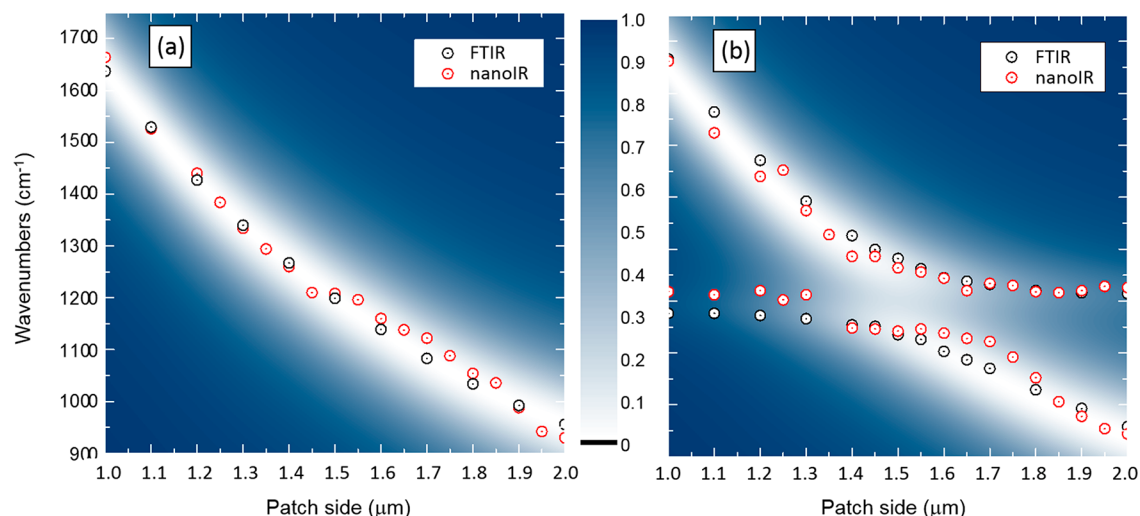
Figure 3. Cavity resonances peak position as a function of patch side *L* extracted from the FTIR (black symbols) and T2Nano-IR (red symbols) spectra in Figure 2. Note that FTIR absorption is obtained from an ensemble of identical cavities on a 100 × 100 *μ*m area while T2Nano-IR photoexpansion peaks are obtained on single cavity resonators. The color map in the background is the expected absorption, calculated analytically by coupled mode theory; (a): undoped QW, (b): doped QW.
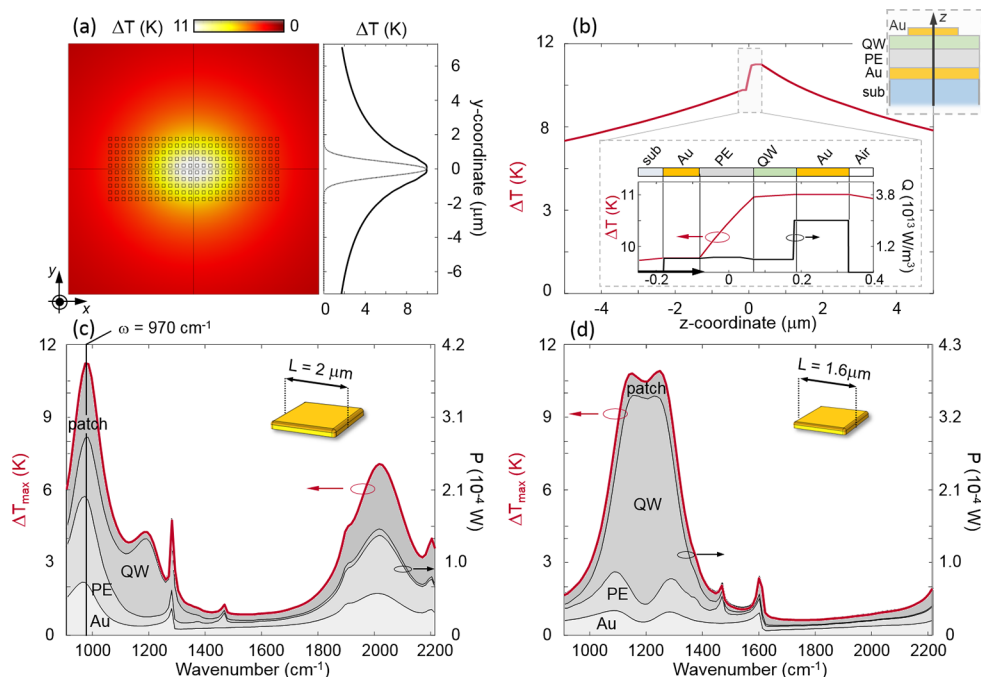

Figure 4. (a) Spatial distribution of the simulated temperature increase **Δ***T*, shown across a (*x*,*y*) cross section of the sample upon illumination at *λ* = 10.31 *μ*m (Gaussian beam parameters considered as in the main text, patch side *L* = 2 *μ*m). In the inset the spatial profile of the temperature increase within the QW layer is evaluated as a vertical cut of the 2D map at *x* = 0, as a function of the *y*-coordinate (thick solid line), and is compared to the laser intensity profile (thin dotted line). (b) Spatial profile of the simulated temperature increase **Δ***T* evaluated along the vertical line (*z*) that runs across the device structure on a mm range, i.e. from the silica substrate to the air above of one of the central patches (see top-right sketch). The panel inset shows (red line, left axis) a zoom-in of the temperature increase across the nanocavity structure only. The power density *Q* (in W/m³) dissipated in each layer is also shown (black curve, right axis) along the same vertical line. (c) Spectrum of the simulated maximum temperature increase (red-line, left axis) reached within the active region for a sample with the patch side *L* = 2 *μ*m, as a function of the illumination wavenumber. On the right axis, the total heat power is disentangled in the dissipation contributions due to single heat sources (black lines and shaded areas with relative labels). (d) Same as for panel c for a patch side *L*= 1.6 *μ*m, when heat dissipation is predicted to be dominated by the contribution arising indeed from the QW (note the much larger relative shaded area ascribed to the power dissipated by the QW).

specific local value of Δ*T* in the PE layer, which is determined by the thermal transduction process, i.e. by the detailed geometry and thermal conductance of each layer and interface. A finite-element method (FEM)-based model has been developed, accounting for the optical and thermal response of the nanocavity components (from top to bottom: the Au patch, the active doped QW layer, the PE layer and the Au ground plane, lying on a glass substrate in air).

Details of our modeling approach implementation can be found in the Supporting Information. The main results of our numerical simulations are reported in Figure 4 for the two prototypical samples with square patch side L = 2.0 μm (far from the anticrossing point) and L = 1.6 μm (at the anticrossing point). The illumination conditions driving the heat dissipation across the system mimic the T2NanoIR configuration: a p-polarized Gaussian beam focus with full width of 25 μm (10 μm) in the x (y) direction and 800 μW of average power impinges on the sample with an angle of incidence of 70°. The optical excitation of the cavity produces a dissipation of the electromagnetic power within the different (lossy) components of the structure $Q = \frac{1}{2}Re\{\boldsymbol{E}\cdot\boldsymbol{J}_{\mathrm{D}}^{*}\}$, with the local electric field $\boldsymbol{E}$ inducing a local displacement current density $\boldsymbol{J}_{\mathrm{D}}$. The local Q is distinctly defined in each domain of the numerical FEM geometry, and its volume integral determines the amount of power that promotes heating of the sample, however in order to calculate the local ΔT the heat diffusion problem has to be solved. This has been done here for the case of the large nanocavity array and not for isolated nanocavities for two reasons: (i) we want to be able to compare the simulations with the broader data set of Figure 2; (ii) the local ΔT in the central part of the illumination area of a large array can be considered approximately homogeneous in (x,y) (see Figure 4a) and this simplifies the interpretation of the thermal simulations in terms of z-profiles only. Considering the dimensions of the Gaussian beam, a finite array made of 26 × 10 patches has been solved for the heat diffusion problem.

Figure 4a shows the calculated spatial distribution of ΔT across the structure for a monochromatic excitation at ω = 970 cm^{-1}; an in-plane (x,y) map is shown along a cross section of the sample taken at the center of the QW thickness. Numerical simulations confirm that the (x,y) temperature distribution follows from the laser intensity profile, as shown in the right panel of Figure 4a. Yet, for our investigation, the most relevant information is represented by the z-profile of the temperature increase inside the cavity. To assess its trend, $\Delta T(z)$ was evaluated along a vertical (z) line cutting through all the layers of the central patch. Results in Figure 4b predict that ΔT (average value ~10.5 K) is relatively uniform inside the cavity (inset, red curve), and has a maximum excursion in the PE layer, as expected by design. The inset of Figure 4b also shows the terms of heat dissipation density Q (assumed to be homogeneous in (x,y)) evaluated along the same vertical line (refer to black arrows in the panel inset) arising from each layer: the highest dissipated power density term is ascribed to the Au square patch.

Figure 4b also shows the terms of heat dissipation density (assumed to be homogeneous in (x,y)) evaluated along the same vertical line (refer to black arrows in the panel inset) arising from each layer: the highest dissipated power density term is ascribed to the Au square patch.

Heat dissipation arises from the interaction with the electromagnetic field, hence the thermal response of the structure varies with the considered excitation wavenumber and is demonstrated to be sensitive to the character of the light−matter interaction regime, either far from, or at, the anticrossing point. To illustrate this effect, Figure 4c,d (red curves, left axis) reports the maximum temperature increase evaluated within the active region as a function of the impinging laser wavelength for the two values L = 2.0 and 1.6 μm. Simulations can be compared to the corresponding T2NanoIR spectra in Figure 2. Figure 4c corresponds to a large detuning between cavity and ISB transition, while in Figure 4d the perfect anticrossing point is reached. In both cases, the simulations well reproduce the experimental spectral positions of the peaks, and their relative intensity (dotted lines in panels c and d). Even the SEIRA-like enhancement of the PE vibrational lines at 1370 and 1460 cm^{-1} is reproduced. On the other hand, simulations slightly overestimate the line widths, since they were performed without any fit parameters and considered a standard 10% FWHM for the ISB transition.

The photothermal simulations provide a deeper insight into the origin of the dissipation in the system and highlight the hybrid character of the polaritonic modes. In Figure 4c, the black curves (right axis) and relative shaded areas represent the cumulative dissipated power P (the power density Q integrated over the corresponding component volume), disentangled in terms of contributions arising from the individual heat sources within the different cavity components. Far from the anticrossing, when L = 2.0 μm and the fundamental cavity mode is far from the ISB transition, the interaction is nonresonant and it does not enhance heat dissipation in the QW. On the other hand, at perfect anticrossing (L = 1.6 μm, Figure 4d) the fundamental cavity mode with m = 1 resonates with the ISB transition, enabling the anticrossing behavior and amplifying the heat dissipation in the QW, which interestingly dominates over ohmic dissipation in the metal layers (compare shaded areas in Figure 4d). We also notice that dissipation in the PE layer cannot be considered as totally negligible, due to residual vibrational absorption strength in the polymer and high field enhancement in the cavity. Obviously, using a polymer with vibrational resonances in this wavelength range would lead to a very large SEIRA effect that would obscure any other thermal behavior in the cavity.

In the final part of the work, we investigate if we can resolve different nanoscale fields and/or current patterns connected to the different cavity modes using the T2NanoIR in imaging mode, i.e. acquiring the T2NanoIR signal with the QCL wavelength fixed at the resonant frequency ω_m, while scanning the AFM tip position (x,y) on the surface of the top metal patch. Given the homogeneity of $\Delta T(x,y)$ for each excitation condition discussed in Figure 4, T2NanoIR in imaging mode provides a measurement of the near-field-coupled energy as a function of the gold-coated AFM tip position (x,y). We start from a specific undoped individual resonator with patch side L = 2.0 μm whose T2NanoIR spectrum in Figure 2a shows the m = 1 mode at 970 cm^{-1} and the m = 2 mode at 1850 cm^{-1}. We thus perform T2NanoIR imaging at ω_1 and ω_2. A subset of the pixels inside the patch perimeter has been selected for imaging, corresponding to 90% of the patch area, to avoid measurement artifacts stemming from ascending/descending topography. We obtain the maps in Figure 5a,b for ω_1 and ω_2, respectively. Red pixels correspond to a high signal. The S/N ratio is low due to the strong (x,y)-independent far-field photoexpansion signal discussed in the paper.

Nevertheless, we clearly observe a single lobe at ω_1, and two lobes with a nodal line in the center at ω_2. The one-dimensional (1-D) symmetry of the lobes allows one to sum, over the orthogonal direction y, the T2NanoIR image profiles along x hence obtaining the 1-D intensity profiles shown as plots above the maps. These profiles are reminiscent of a 1-D standing wave pattern corresponding to the electric-current standing waves $\boldsymbol{J}(x)$ in the top metal patch sketched in Figure 1b. Interestingly, in a one-dimensional cavity approximation,

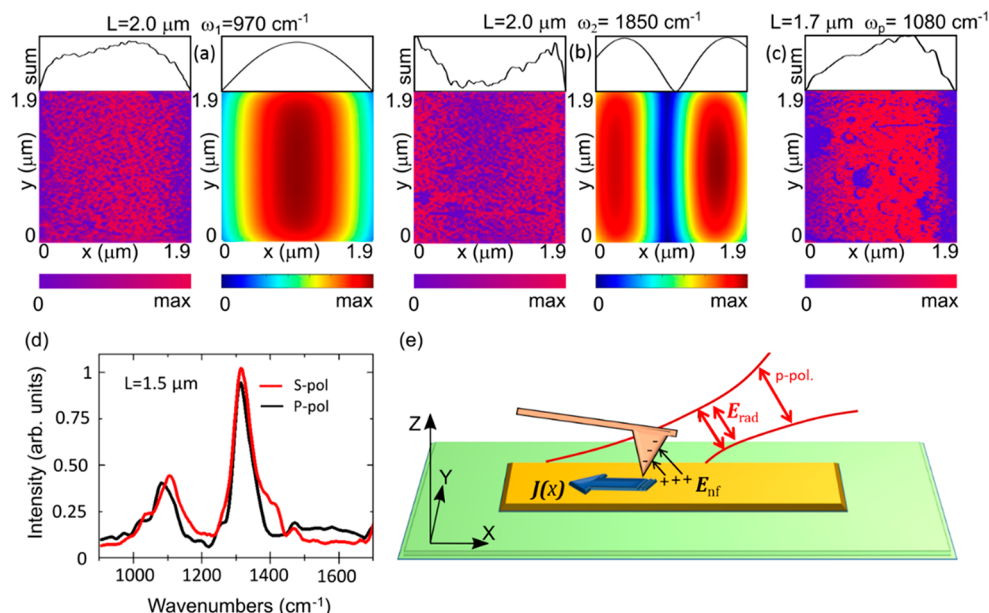**Figure 5.** Near-field imaging of nanoscale patterns on the patch resonator with side L = 2.0 μm top surface for different cavity modes. (a, b) T2NanoIR signal maps (left) and calculated in-plane magnetic field from FDTD simulations (right) at frequencies matching the $m = 1$ (a) and $m = 2$ mode (b), respectively. The top insets are summed line profiles calculated from the corresponding maps. Note that in 1-D approximation the in-plane magnetic field H_y patterns correspond to the electrical current patterns, therefore the mode symmetry is the same for H_y and $J(x)$. Also note that a constant background has been subtracted from the T2NanoIR maps. (c) T2NanoIR signal map taken for a patch resonator with side L = 1.7 μm (thus fully included in the map) for the lower polariton peak frequency $\omega = 1080$ cm^{-1}: a single lobe pattern is observed as for the unperturbed $m = 1$ cavity mode. (d) Comparison of T2Nano-IR spectra acquired on the same patch without moving the AFM tip but rotating the polarization from p to s, thereby eliminating any near-field enhancement by the tip. Due to the square shape of the patch, there is a 90° rotation invariance. The antenna spectrum therefore does not depend on the linear polarization direction: only the action of the tip could have made a difference, but this was not the case. (e) Sketch of the near-field coupling mechanism generating the image contrast in p-polarization. According to this view one can picture the experimental maps in panels a, b, and c as maps of the near-field coupling strength.

the application of the fourth Maxwell's equation $\nabla \times H = J + \varepsilon_0 \, \partial E / \partial t$ shows that the electric-current patterns have the same symmetry as the pattern of the in-plane magnetic field components H_y. These can be easily extracted from EM simulations and are reported in Figure 5a,b. On the other hand, the vertical electric field E_z, which is usually taken as the dominant near-field interaction quantity, e.g., in SNOM experiments,[39] would have $m + 1$ lobes instead of m lobes as it can be inferred from the third Maxwell's equation $\nabla \times E = -\mu_0 \, \partial H / \partial t$ (see the Supporting Information for all the simulated field intensity patterns).

From this observation, we suggest that the metal-coated AFM-tip excites the electric current $J(x)$ on the patch surface through the near-field enhanced component E_x, instead. The excitation of an electric current along x is possible in p-polarization because, at 70° incidence, there is still a minor component of the radiation electric field directed along x, and the electric field enhancement is certainly asymmetric along x,[43] leading to a net charge displacement in one direction as a function of time (see sketch in Figure 5e). The near-field enhancement of E_x can be taken as position-independent within the square patch area far from the edges, but the available effective conductivity of the patch depends on x through the standing wave relation $J(x) = J_{max}\sin(m\pi x/L)$. In this respect, the electric current standing wave pattern behaves like a local density of optical states (LDOS) usually defined in scattering-SNOM problems,[44] although this is only a similarity and the two concepts are well separated.

In Figure 5c, we perform a similar mapping analysis of a doped-QW patch close to the anticrossing point with L = 1.7 μm. We use a laser wavenumber $\omega_{pol} = 1080$ cm^{-1} corresponding to the lower polariton peak frequency, which, because of the anticrossing behavior, is frequency-shifted with respect to the $m = 1$ mode of the corresponding undoped QW around 1180 cm^{-1}. Nevertheless, the electric-current standing-wave symmetry of the lower polariton resonance mirrors the one-lobe symmetry of the $m = 1$ fundamental mode of the undoped QW patch of Figure 5(a). This behavior can be easily understood even in a semiclassical framework for polariton splitting theory, where the ISB transition is modeled as a Lorentzian resonance that leads to a strong modification of the value of the effective refractive index from the quasi ω-independent value of the undoped QW.[42] In other words, the one-dimensional mode equation $\omega_m = 4\pi c/nmL$ also holds for polariton modes if a suitable effective index is used in substitution of the refractive index of the dielectric-loaded cavity.

As anticipated, in the present case of strong light−matter interaction in square patches, the magnitude of the near-field tip-coupled energy is much smaller than the energy directly coupled by the free-space laser radiation into the patch. The spectral efficiency of the tip-coupling mechanism is almost flat, as further demonstrated in Figure 5d by the two T2NanoIR spectra taken on the same patch (L = 1.5 μm shown as an example) and without moving the gold-coated AFM tip by simply rotating the polarization from p to s through a periscope. Changes shown in Figure 5d are interpreted as

minor modifications due to slightly different in-coupling geometry. While a full study of the near-field coupling mechanism is beyond the scope of this paper, our suggested interpretation of the imaging contrast mechanism in terms of excitation of the local electric current standing wave is supported by two initial tests: (i) cavity mode imaging by using a dielectric tip, and (ii) cavity mode imaging with s-polarization while still using a metal-coated tip. In both cases, no imaging contrast was observed: indeed, the dielectric tip does not couple to the electric current, and an electric field in s-polarized radiation cannot produce an asymmetric field enhancement along y (if any) because it is orthogonal to both the tip axis (z) and the incidence plane (xz). This finding confirms the added near-field mapping capability of T2NanoIR in the case of gold-coated tips and p-polarized laser illumination, which is also the most common configuration for nano-IR spectroscopy instruments. Importantly, it reveals that the T2NanoIR maps do not represent the local heating in each xy position inside the cavity, as in this case we would have observed patterns corresponding to the local E_z field distribution. Instead, they represent a map of the near-field coupling strength between the patch and the tip apex, which is found to be higher where the EM field component H_y (hence the electric current $J(x)$) is more intense.

CONCLUSIONS

In summary, we have demonstrated an original technique, the thermal-transducer-NanoIR (T2NanoIR), that permits the study of the light−matter interaction inside single isolated nanocavities. It relies on the insertion of a nonperturbative polymer transducer in the cavity that permits the detection of the absorbed optical power in the form of thermal expansion driven by optical energy dissipation into heat. The ability of T2Nano-IR to measure optical energy dissipation at the nanoscale, coupled to the predictive character of the thermal simulations, could enable in the future the individual measurement of the contributions of the different dissipation channels, even in complex sample geometries. This could help design optimization: for instance, in detectors solely the losses in the active region yield a signal, while all the other dissipation channels are of course unwanted.

EXPERIMENTAL METHODS

Materials. The samples are doped InGaAs/AlInAs semiconductor QWs epitaxially grown by MBE on low-doped InP substrates. The undoped sample contains three 10.5 nm-thick QWs separated by 15 nm-thick barriers, for a total epitaxial thickness of 151.5 nm, while the doped sample is a single multisubband plasmon quantum well, made of a 18.5 nm thick well, Si-doped to 10^{18} cm^{-3} and surrounded by InGaAs barriers for a total thickness of 112 nm. Products for the deposition of polyethylene (HDPE powder and decahydronaphtha-lene solvent) were purchased by Sigma-Aldrich. The full fabrication sequence and methods are described in the first Supporting Information section.

Characterization. Far-field characterization was carried out using a Thermo Nicolet Nexus 870 FTIR connected to a microscope unit (Nicolet Continuum) equipped with a 32× Cassegrain objective. Illumination was provided with a globar source and measurements performed in reflectivity configuration, detecting the optical response with a cooled MCT detector. AFM-IR measurements were performed using a NanoIR2 (Bruker - Anasys Instruments), purging with dry air both the optics and the sample compartment for many hours. The beam from a broadly tunable mid-IR QCL (MIRCATxB, Daylight Solutions, with a spectral range 900−1800 cm^{-1}) was tightly focused onto the gold-coated tip of an AFM probe. In p-polarization, the IR beam impinges from the side at an angle of 70° to the surface normal, that is, with the electric field oriented at 20° with surface normal. In s-polarization, obtained by inserting a custom reflective periscope between the laser and the NanoIR2 and then using the same optical path, the electric field is parallel to the surface. The laser provided 260 ns long light pulses at a repetition frequency in resonance with the second mechanical bending mode of the cantilever at ∼200 kHz (resonantly enhanced infrared nanospectroscopy, REINS). The laser power was adjusted using transmission metal-mesh filters in front of the QCL output and it was in the range 1−50 mW depending on frequency range and sample absorption. The laser spectrum is measured with a pyroelectric detector and used as a reference for the incoming laser power.

ASSOCIATED CONTENT

ⓢ Supporting Information

The Supporting Information is available free of charge at https://pubs.acs.org/doi/10.1021/acsnano.2c04452.

> (i) Detailed device fabrication steps; (ii) details of the employed simulation model (COMSOL) and extension of calculated results for a highly thermally conductive substrate; (iii) simulated electromagnetic patterns of the photonic cavity modes; (iv) a comparison between SNOM and T2NanoIR measurements, showing the unambiguity of results from the latter; (v) considerations on reproducibility (different devices and different active regions) (PDF)

AUTHOR INFORMATION

Corresponding Authors

Mario Malerba − Centre de Nanosciences et de Nanotechnologies (C2N), CNRS UMR 9001, Université Paris-Saclay, 91120 Palaiseau, France; ⓘ orcid.org/0000-0003-0553-2770; Email: mario.malerba@c2n.upsaclay.fr

Michele Ortolani − Department of Physics, Sapienza University of Rome, 00185 Rome, Italy; Center for Life NanoScience, Istituto Italiano di Tecnologia, 00161 Rome, Italy; ⓘ orcid.org/0000-0002-7203-5355; Email: michele.ortolani@uniroma1.it

Raffaele Colombelli − Centre de Nanosciences et de Nanotechnologies (C2N), CNRS UMR 9001, Université Paris-Saclay, 91120 Palaiseau, France; Email: raffaele.colombelli@c2n.upsaclay.fr

Authors

Simone Sotgiu − Department of Physics, Sapienza University of Rome, 00185 Rome, Italy; ⓘ orcid.org/0000-0001-7889-9763

Andrea Schirato − Dipartimento di Fisica, Politecnico di Milano, 20133 Milan, Italy; Istituto Italiano di Tecnologia, 16163 Genoa, Italy

Leonetta Baldassarre − Department of Physics, Sapienza University of Rome, 00185 Rome, Italy; ⓘ orcid.org/0000-0003-2217-0564

Raymond Gillibert − Center for Life NanoScience, Istituto Italiano di Tecnologia, 00161 Rome, Italy; ⓘ orcid.org/0000-0003-4318-6346

Valeria Giliberti − Center for Life NanoScience, Istituto Italiano di Tecnologia, 00161 Rome, Italy

Mathieu Jeannin − Centre de Nanosciences et de Nanotechnologies (C2N), CNRS UMR 9001, Université Paris-Saclay, 91120 Palaiseau, France; ⓘ orcid.org/0000-0001-8878-8960

Jean-Michel Manceau − *Centre de Nanosciences et de Nanotechnologies (C2N), CNRS UMR 9001, Université Paris-Saclay, 91120 Palaiseau, France*

Lianhe Li − *School of Electronic and Electrical Engineering, University of Leeds, LS29JT Leeds, United Kingdom;* ⊙ orcid.org/0000-0003-4998-7259

Alexander Giles Davies − *School of Electronic and Electrical Engineering, University of Leeds, LS29JT Leeds, United Kingdom*

Edmund H. Linfield − *School of Electronic and Electrical Engineering, University of Leeds, LS29JT Leeds, United Kingdom*

Alessandro Alabastri − *Department of Electrical and Computer Engineering, Rice University, Houston, Texas 77005, United States;* ⊙ orcid.org/0000-0001-6180-8052

Complete contact information is available at:
https://pubs.acs.org/10.1021/acsnano.2c04452

Author Contributions

¶M.M. and S.S. contributed equally.

Notes

The authors declare no competing financial interest.

REFERENCES

(1) Shelby, R. A.; Smith, D. R.; Schultz, S. Experimental verification of a negative index of refraction. *Science* 2001, 292, 77.

(2) Yu, N.; Genevet, P.; Kats, M. A.; Aieta, F.; Tetienne, J.-P.; Capasso, F.; Gaburro, Z. Light propagation with phase discontinuities: generalized laws of reflection and refraction. *Science* 2011, 334, 333−7.

(3) Kildishev, A. V.; Boltasseva, A.; Shalaev, V. M. Planar Photonics with Metasurfaces. *Science* 2013, 339, 1232009.

(4) Lee, J.; Nookala, N.; Gomez-Diaz, J. S.; Tymchenko, M.; Demmerle, F.; Boehm, G.; Amann, M. C.; Alù, A.; Belkin, M. A. Ultrathin Second-Harmonic Metasurfaces with Record-High Nonlinear Optical Response. *Adv. Opt. Mater.* 2016, 4, 664.

(5) Yu, N.; Capasso, F. Flat optics with designer metasurfaces. *Nat. Mater.* 2014, 13, 139−150.

(6) Neshev, D.; Aharonovich, I. Optical metasurfaces: new generation building blocks for multi-functional optics. *Light Sci. Appl.* 2018, 7, 58.

(7) Schirato, A.; Maiuri, M.; Toma, A.; Fugattini, S.; Proietti Zaccaria, R.; Laporta, P.; Nordlander, P.; Cerullo, G.; Alabastri, A.; Della Valle, G. Transient optical symmetry breaking for ultrafast broadband dichroism in plasmonic metasurfaces. *Nat. Photonics* 2020, 14, 723−727.

(8) Khanikaev, A. B.; Arju, N.; Fan, Z.; Purtseladze, D.; Lu, F.; Lee, J.; Sarriugarte, P.; Schnell, M.; Hillenbrand, R.; Belkin, M. A.; Shvets, G. Experimental demonstration of the microscopic origin of circular dichroism in two-dimensional metamaterials. *Nat. Commun.* 2016, 7, 12045.

(9) Rajabali, S.; Markmann, S.; Jöchl, E.; Beck, M.; Lehner, C. A.; Wegscheider, W.; Faist, J.; Scalari, G. An ultrastrongly coupled single THz meta-atom. *Nat. Commun.* 2022, 13, 2528.

(10) Nga Chen, Y.; Todorov, Y.; Askenazi, B.; Vasanelli, A.; Biasiol, G.; Colombelli, R.; Sirtori, C. Antenna-coupled microcavities for enhanced infrared photo-detection. *Appl. Phys. Lett.* 2014, 104, 031113.

(11) Hakl, M.; Lin, Q.; Lepillet, S.; Billet, M.; Lampin, J.-F.; Pirotta, S.; Colombelli, R.; Wan, W.; Cao, J. C.; Li, H.; Peytavit, E.; Barbieri, S. Ultrafast Quantum-Well Photodetectors Operating at 10 μm with a Flat Frequency Response up to 70 GHz at Room Temperature. *ACS Photonics* 2021, 8, 464−471.

(12) Xu, L.; Curwen, C. A.; Reno, J. L.; Williams, B. S. High performance terahertz metasurface quantum-cascade VECSEL with an intra-cryostat cavity. *Appl. Phys. Lett.* 2017, 111, 101101.

(13) Pirotta, S.; Tran, N.-L.; Jollivet, A.; Biasiol, G.; Crozat, P.; Manceau, J.-M.; Bousseksou, A.; Colombelli, R. Fast amplitude modulation up to 1.5 GHz of mid-IR free-space beams at room-temperature. *Nat. Commun.* 2021, 12, 799.

(14) De Liberato, S.; Ciuti, C.; Carusotto, I. Quantum vacuum radiation spectra from a semiconductor microcavity with a time-modulated vacuum Rabi frequency. *Phys. Rev. Lett.* 2007, 98, 103602.

(15) Knorr, M.; Manceau, J. M.; Mornhinweg, J.; Nespolo, J.; Biasiol, G.; Tran, N. L.; Malerba, M.; Goulain, P.; Lafosse, X.; Jeannin, M.; Stefinger, M.; Carusotto, I.; Lange, C.; Colombelli, R.; Huber, R. Intersubband polariton-polariton scattering in a dispersive microcavity. *Phys. Rev. Lett.* 2022, 128, 247401.

(16) Dini, D.; Köhler, R.; Tredicucci, A.; Biasiol, G.; Sorba, L. Microcavity Polariton Splitting of Intersubband Transitions. *Phys. Rev. Lett.* 2003, 90, 116401.

(17) Vigneron, P. B.; Pirotta, S.; Carusotto, I.; Tran, N. L.; Biasiol, G.; Manceau, J. M.; Bousseksou, A.; Colombelli, R. Quantum well infrared photo-detectors operating in the strong light-matter coupling regime. *Appl. Phys. Lett.* 2019, 114, 131104.

(18) Mann, S. A.; Nookala, N.; Johnson, S. C.; Cotrufo, M.; Mekawy, A.; Klem, J. F.; Brener, I.; Raschke, M. B.; Alù, A.; Belkin, M. A. Ultrafast optical switching and power limiting in intersubband polaritonic metasurfaces. *Optica* 2021, 8, 606.

(19) Balanis, C. *Antenna Theory: Analysis and Design*; John Wiley and Sons Inc.: Hoboken, NJ, 2005.

(20) Li, C.; Krachmalnicoff, V.; Bouchon, P.; Jaeck, J.; Bardou, N.; Haïdar, R.; De Wilde, Y. Near-Field and Far-Field Thermal Emission of an Individual Patch Nanoantenna. *Phys. Rev. Lett.* 2018, 121, 243901.

(21) Wang, C. F.; Habteyes, T. G.; Luk, T. S.; Klem, J. F.; Brener, I.; Chen, H. T.; Mitrofanov, O. Observation of Intersubband Polaritons in a Single Nanoantenna Using Nano-FTIR Spectroscopy. *Nano Lett.* 2019, 19, 4620−4626.

(22) Gillibert, R.; Malerba, M.; Spirito, D.; Giliberti, V.; Li, L.; Davies, A. G.; Linfield, E. H.; Baldassarre, L.; Colombelli, R.; Ortolani, M. Nanospectroscopy of a single patch antenna strongly coupled to a mid-infrared intersubband transition in a quantum well. *Appl. Phys. Lett.* 2020, 117, 101104.

(23) Benz, A.; Campione, S.; Liu, S.; Montaño, I.; Klem, J. F.; Allerman, A.; Wendt, J. R.; Sinclair, M. B.; Capolino, F.; Brener, I. Strong coupling in the sub-wavelength limit using metamaterial nanocavities. *Nat. Commun.* 2013, 4, 2882.

(24) Dazzi, A.; Glotin, F.; Carminati, R. Theory of infrared nanospectroscopy by photothermal induced resonance. *J. Appl. Phys.* 2010, 107, 124519.

(25) Lu, F.; Jin, M.; Belkin, M. A. Tip-enhanced infrared nanospectroscopy via molecular expansion force detection. *Nat. Photonics* 2014, 8, 307−312.

(26) Chae, J.; Lahiri, B.; Centrone, A. Engineering Near-Field SEIRA Enhancements in Plasmonic Resonators. *ACS Photonics* **2016**, *3*, 87−95.

(27) Mancini, A.; Giliberti, V.; Alabastri, A.; Calandrini, E.; De Angelis, F.; Garoli, D.; Ortolani, M. Thermoplasmonic Effect of Surface-Enhanced Infrared Absorption in Vertical Nanoantenna Arrays. *J. Phys. Chem. C* **2018**, *122*, 13072−13081.

(28) Helm, M.The Basic Physics of Intersubband Transitions. In *Intersubband Transitions in Quantum Wells: Physics and Device Applications I*; Liu, H. C., Capasso, F., Eds.; Academic Press: London, 2000.

(29) Yao, Y.; Hoffman, A. J.; Gmachl, C. F. Mid-infrared quantum cascade lasers. *Nat. Photonics* **2012**, *6*, 432−439.

(30) Weber, E. R.; Willardson, R. K.; Liu, H. C.; Capasso, F.*Intersubband Transitions in Quantum Wells: Physics and Device Applications*; Academic Press: London, 1999.

(31) Weisbuch, C.; Nishioka, M.; Ishikawa, A.; Arakawa, Y. Observation of the coupled exciton-photon mode splitting in a semiconductor quantum microcavity. *Phys. Rev. Lett.* **1992**, *69*, 3314.

(32) Sapienza, L.; Vasanelli, A.; Colombelli, R.; Ciuti, C.; Chassagneux, Y.; Manquest, C.; Gennser, U.; Sirtori, C. Electrically Injected Cavity Polaritons. *Phys. Rev. Lett.* **2008**, *100*, 136806.

(33) Geiser, M.; Scalari, G.; Castellano, F.; Beck, M.; Faist, J. Room temperature terahertz polariton emitter. *Appl. Phys. Lett.* **2012**, *101*, 141118.

(34) Günter, G.; Anappara, A. A.; Hees, J.; Sell, A.; Biasiol, G.; Sorba, L.; De Liberato, S.; Ciuti, C.; Tredicucci, A.; Leitenstorfer, A.; Huber, R. Sub-cycle switch-on of ultrastrong light-matter interaction. *Nature* **2009**, *458*, 178−181.

(35) Scalari, G.; Maissen, C.; Turčinková, D.; Hagenmüller, D.; De Liberato, S.; Ciuti, C.; Reichl, C.; Schuh, D.; Wegscheider, W.; Beck, M.; Faist, J. Ultrastrong Coupling of the Cyclotron Transition of a 2D Electron Gas to a THz Metamaterial. *Science* **2012**, *335*, 1323.

(36) Todorov, Y.; Andrews, A. M.; Colombelli, R.; De Liberato, S.; Ciuti, C.; Klang, P.; Strasser, G.; Sirtori, C. Ultrastrong Light-Matter Coupling Regime with Polariton Dots. *Phys. Rev. Lett.* **2010**, *105*, 196402.

(37) Lagrée, M.; Jeannin, M.; Quinchard, G.; Ouznali, O.; Evirgen, A.; Trinité, V.; Colombelli, R.; Delga, A. Direct polariton-to-electron tunneling in quantum cascade detectors operating in the strong light-matter coupling regime. *Phys. Rev.* **2022**, *17*, 044021.

(38) Boneberg, J.; Koenig-Birk, J.; Muenzer, H.-J.; Leiderer, P.; Shuford, K. L.; Schatz, G. C. Optical near-fields of triangular nanostructures. *Appl. Phys. A: Mater. Sci. Process.* **2007**, *89*, 299.

(39) Leiderer, P.; Bartels, C.; König-Birk, J.; Mosbacher, M.; Boneberg, J. Imaging optical near-fields of nanostructures. *Appl. Phys. Lett.* **2004**, *85*, 5370.

(40) Volpe, G.; Noack, M.; Aćimović, S. S.; Reinhardt, C.; Quidant, R. Near-field mapping of plasmonic antennas by multiphoton absorption in poly (methyl methacrylate). *Nano Lett.* **2012**, *12*, 4864.

(41) Muller, E. A.; Pollard, B.; Bechtel, H. A.; Adato, R.; Etezadi, D.; Altug, H.; Raschke, M. B. Nanoimaging and Control of Molecular Vibrations through Electromagnetically Induced Scattering Reaching the Strong Coupling Regime. *ACS Photonics* **2018**, *5* (9), 3594−3600.

(42) Todorov, Y.; Tosetto, L.; Teissier, J.; Andrews, a M.; Klang, P.; Colombelli, R.; Sagnes, I.; Strasser, G.; Sirtori, C. Optical properties of metal-dielectric-metal microcavities in the THz frequency range. *Opt. Express* **2010**, *18*, 13886−13907.

(43) Roth, R. M.; Panoiu, N. C.; Adams, M. M.; Osgood, R. M.; Neacsu, C. C.; Raschke, M. B. Resonant-plasmon field enhancement from asymmetrically illuminated conical metallic-probe tips. *Optics Express* **2006**, *14*, 2921−2931.

(44) Joulain, K.; Carminati, R.; Mulet, J.-P.; Greffet, J.-J. Definition and Measurement of the Local Density of Electromagnetic States close to an interface. *Phys. Rev. B* **2003**, *68*, 245405.